Hybrid normal-superconducting Aharonov-Bohm quantum thermal device

IOP Publishing Quantum Sci. Technol. 8 (2023) 015023 https://doi.org/10.1088/2058-9565/acacbf

Quantum Science and Technology

OPEN ACCESS

RECEIVED
9 September 2022

REVISED
19 November 2022

ACCEPTED FOR PUBLICATION
19 December 2022

PUBLISHED
30 December 2022

PAPER

Hybrid normal-superconducting Aharonov-Bohm quantum thermal device

Gianmichele Blasi[1,*], **Francesco Giazotto**[2] and **Géraldine Haack**[1]

[1] Department of Applied Physics, Université de Genève, Geneva 1211, Switzerland
[2] NEST, Instituto Nanoscienze-CNR and Scuola Normale Superiore, Piazza San Silvestro 12, Pisa 56127, Italy
[*] Author to whom any correspondence should be addressed.

E-mail: gianmichele.blasi@unige.ch

Keywords: Aharonov-Bohm, quantum heat engine, quantum thermal rectifier, superconducting, phase-coherent caloritronics

Abstract

We propose and theoretically investigate the behavior of a ballistic Aharonov-Bohm (AB) ring when embedded in a N-S two-terminal setup, consisting of a normal metal (N) and superconducting (S) leads. This device is based on available current technologies and we show in this work that it constitutes a promising hybrid quantum thermal device, as a quantum heat engine and quantum thermal rectifier. Remarkably, we evidence the interplay of single-particle quantum interferences in the AB ring and of the superconducting properties of the structure to achieve the hybrid operating mode for this quantum device. Its efficiency as a quantum heat engine reaches 55% of the Carnot efficiency, and we predict a thermal rectification factor attaining 350%. These results make this device highly promising for future phase-coherent caloritronic nanodevices.

1. Introduction

Engineering versatile and efficient quantum thermal devices to manage heat at the nanoscale is highly challenging and relevant for future quantum technologies [1–3]. Controlling heat implies, in particular, being able to exploit a temperature gradient as a resource for operating a device as heat engine [4–9], and to allow for preferential heat flow in one direction under thermal biasing, a feature known as thermal rectification [1, 10, 11]. Both abilities have been investigated independently from each other, motivating numerous proposals and experiments that exploit various platforms with the objective of managing heat at the nanoscale in an efficient way. As recent examples, we emphasize achievements with superconducting circuit QED setups [10, 12, 13], with superconducting-semiconducting devices [14–16] and with graphene-based samples [17] for heat rectification. The first experimental heat engines at the nanoscale have exploited among others features trapped ions [18, 19] and cold atoms [20], NV-centers samples [21], semiconducting quantum dots [5] and, very recently, superconducting tunnel junctions [7].

Towards the development of realistic and efficient quantum technologies, it becomes clear that hybrid quantum thermal devices that can combine several tasks towards heat management at the nanoscale become highly desirable. Their characterization has been the topic of recent theoretical investigations [22–26]. Here, we propose and theoretically investigate an Aharonov-Bohm (AB) ring embedded in a normal-superconducting (N-S) two-terminal device as a versatile and efficient quantum thermal machine. We demonstrate that both single-quantum interferences and superconducting contact allow for operating this device as a quantum heat engine and a quantum heat rectifier. This configuration is inspired by recent works demonstrating on the one side, excellent thermoelectric response of an AB ring in a normal two-terminal setup [27, 28] and on the other side, high rectification coefficients by exploiting a left-right asymmetry in the density of states (DOSs) of the contacts induced by the superconducting gap compared to the normal metal [1]. From a theoretical point of view, we characterize the behavior of this N-S AB interferometer within and beyond the Andreev approximation, evaluating the functioning of N-S structures as quantum thermal devices in full generality.

2. Theoretical framework

We analyze the thermodynamic performances of an AB ring in an N-S two-terminal setup within a scattering-matrix formalism [29]. This theoretical approach is motivated by its ability to keep track of the quasiparticles phase coherence in the device and of the specificities of the superconducting contact characterized by its gap Δ and its critical temperature T_C. In contrast to previous works [27, 28] investigating the AB ring as an efficient thermoelectric device when connected to two normal contacts, we account for the electron-like and hole-like behaviors of the quasiparticles being subject to a temperature bias between the two contacts, one normal metal contact and one superconducting contact. It is the combination of these N-S contacts and the AB ring that allows this device to become hybrid—it acts as heat rectifier and heat engine with large efficiency in both operating modes.

2.1. Model for a N-S AB ring

The device is sketched in figure 1: it is made of an AB ring as central part, connected to the left and right contacts, a normal contact (N) and a superconducting contact (S). The two contacts are described through their chemical potential $\mu_{N,S}$ and temperature $T_{N,S}$. The AB ring encloses a magnetic flux Φ, and is characterized by the length of its upper and lower arms, respectively L_u and L_ℓ. A top gate allows for a gate voltage V_g. The AB ring is connected to the two leads through T-junctions characterized by their transmission probability $\tau \in [0,1]$ [30]. The superconducting contact is connected to the central part through an normal-superconductor (N-S) junction. We model this junction with a delta-like contact resistance at the interface between the normal and superconducting parts, following references [31, 32]. This barrier is characterized by a dimensionless parameter Z: for $Z \ll 1$, the interface is said to be very transparent and ideal for $Z = 0$, whereas $Z \gg 1$ corresponds to the tunnel limit.

Within a scattering matrix approach, we evaluate the charge and heat currents in the normal (left) contact, denoted as I_N and J_N respectively. They can be expressed in the compact form [33–36]:

$$\begin{bmatrix} I_N \\ J_N \end{bmatrix} = \frac{2}{h} \sum_{\substack{j=N,S \\ \alpha,\beta=\pm}} \int_0^\infty \mathrm{d}\epsilon \begin{bmatrix} \alpha e \\ (\epsilon - \alpha\mu_N) \end{bmatrix} \left(f_N^\alpha(\epsilon) - f_j^\beta(\epsilon) \right) \left| \mathcal{S}_{Nj}^{\alpha\beta}(\epsilon) \right|^2 . \tag{1}$$

Here the factor 2 accounts for spin degeneracy, e is the electrical charge, and we define the zero of energy as being that of the electrochemical potential of the superconductor, i.e. $\mu_S = 0$. μ_N is the electrochemical potential of the normal contact [31, 34]. The labels $\alpha, \beta = \pm$ accounts for the electron-like $(+)$ or hole-like $(-)$ quasiparticle, $f_S^\alpha(\epsilon)$ and $f_N^\alpha(\epsilon)$ are respectively the energy-dependent Fermi distributions characterizing the superconducting and normal contacts. Depending on whether the quasiparticle behaves as an electron ($\alpha = +$) or a hole ($\alpha = -$), the electrochemical potential μ_i of lead $i = N, S$ has to be subtracted (electron) or added (hole) to the energy ϵ:

$$f_i^\alpha(\epsilon) = \{ e^{(\epsilon - \alpha\mu_i)/k_B T_i} + 1 \}^{-1}, \tag{2}$$

with T_i the temperature of lead $i = N, S$ and k_B the Boltzmann constant. In equation (1), $\mathcal{S}$ represents the scattering matrix of the whole device, which we now make explicit.

2.2. Scattering matrix of a N-S AB ring

The total scattering matrix (s-matrix) $\mathcal{S}$ for this N-S AB ring is the composition of the s-matrix for the AB ring S_{AB} and the s-matrix of the N-S interface S_{NS} through established rules that conserve the number of quasiparticles flowing through the device [37, 38]:

$$\mathcal{S} = S_{AB} \circ S_{NS}. \tag{3}$$

The s-matrix S_{NS} must account for Andreev reflections [39], allowing an electron to be reflected as a hole and vice-versa. Hence, for a two-terminal device with a single channel, it imposes the form of a 4×4 matrix to $\mathcal{S}, S_{AB}$ and S_{NS}. As the AB ring does not involve any superconducting material, S_{AB} will take a block-diagonal form, indicating that the AB ring does not couple electrons and holes. The matrix S_{AB} depends in general on energy, denoted ϵ below, and can then be written as:

$$S_{AB}(\epsilon) = \begin{pmatrix} r_{AB}^{ee}(\epsilon) & 0 & t_{AB}'^{ee}(\epsilon) & 0 \\ 0 & r_{AB}^{hh}(\epsilon) & 0 & t_{AB}'^{hh}(\epsilon) \\ t_{AB}^{ee}(\epsilon) & 0 & r_{AB}'^{ee}(\epsilon) & 0 \\ 0 & t_{AB}^{hh}(\epsilon) & 0 & r_{AB}'^{hh}(\epsilon) \end{pmatrix}. \tag{4}$$

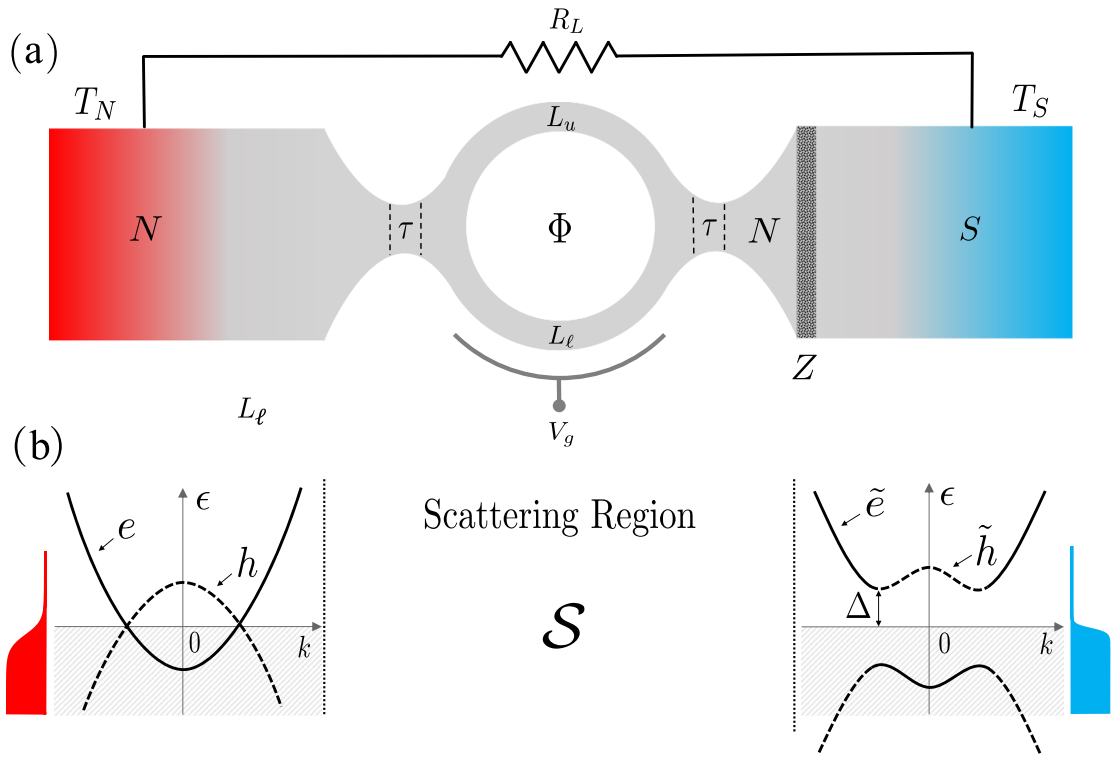

Figure 1. Two-terminal N-S AB quantum thermal device. (a) Scheme of the central AB ring with magnetic flux Φ, gate voltage V_g and length imbalance $\Delta L = L_u - L_\ell$ as tunable parameters. The AB ring is connected to the contacts through two T-junctions with transmission probability τ, and through a N-S junction with the superconducting contact. The N and S contacts are biased in temperature, $T_N - T_S = \Delta T$. The circuit can be closed with dissipationless (superconducting) wires with a load resistance R_L to operate the device as quantum heat engine. (b) Dispersion curves for electron-like quasiparticles (solid curves) and hole-like quasiparticles (dashed curves) respectively in the normal lead (left) and superconducting lead (right). The presence of the superconductor opens a gap Δ in the eigenspectrum, and hybridizes electron- and hole-states. $\mathcal{S}$ indicates the scattering matrix describing the central scattering region accounting for the presence of the AB ring, the T-junctions and the N-S interface.

S_{AB} results from the combination of the s-matrices of the central ring and of the two T-junctions, see appendix A for all details. For a normal metal, the reflection and transmission amplitudes for electrons and holes in equation (4) are simply related through electron–hole conjugation rules:

$$r_{AB}^{hh}(\epsilon) = \left(r_{AB}^{ee}(-\epsilon)\right)^*; \quad t_{AB}^{hh}(\epsilon) = \left(t_{AB}^{ee}(-\epsilon)\right)^*, \tag{5}$$

and similarly for the amplitudes r' and t' for incoming waves from the right. In contrast to S_{AB}, the s-matrix S_{NS} is characterized by non-vanishing off-diagonal elements to account for Andreev processes (allowing an electron to be reflected/transmitted as a hole and vice-versa):

$$S_{NS} = \begin{pmatrix} r_{ee} & r_{eh} & t_{e\tilde{e}} & t_{e\tilde{h}} \\ r_{he} & r_{hh} & t_{h\tilde{e}} & t_{h\tilde{h}} \\ t_{\tilde{e}e} & t_{\tilde{e}h} & r_{\tilde{e}\tilde{e}} & r_{\tilde{e}\tilde{h}} \\ t_{\tilde{h}e} & t_{\tilde{h}h} & r_{\tilde{h}\tilde{e}} & r_{\tilde{h}\tilde{h}} \end{pmatrix}. \tag{6}$$

The reflection and transmission amplitudes for electron, holes and Andreev processes are derived within a Bogoliubov-de Gennes (BdG) formalism to capture the essence of superconductivity [31, 36]. The amplitudes $r_{\alpha\beta}$ and $t_{\alpha\beta}$ represent respectively the reflection and transmission amplitudes of an incoming quasiparticle of type $\beta = e, h$ ($\beta = \tilde{e}, \tilde{h}$) injected from lead N (S) to end up as a quasiparticle of type $\alpha = e, h$ ($\alpha = \tilde{e}, \tilde{h}$) in lead N (S). For clarity, the tilde denotes the quasiparticles in the superconducting lead, $\tilde{e}$ for electron-like and $\tilde{h}$ for hole-like quasiparticles, see figure 1(b). Let us remark that in the limit of a vanishing superconducting gap, $\Delta \to 0$, one recovers the scattering amplitudes derived in previous references investigating a AB ring in a two-terminal device with two normal contacts [27, 28].

Usually, in the literature, the amplitudes in equation (6) are obtained in the so-called Andreev approximation regime, defined when the superconducting gap is much smaller than the Fermi energy, $\Delta \ll \epsilon_F$ [31, 40]. In this case, the scattering amplitudes take a simple analytical form that depends explicitly

on Δ and on the transparency coefficient Z, as we detailed in appendix B. However, it is important to notice that, within the Andreev approximation, all the details about the curvature of the BdG eigenspectrum are lost and, as a result, thermoelectric effects get strongly suppressed. Therefore, to evidence the thermoelectric feature of our hybrid superconducting system, in the following section we will go beyond the Andreev approximation. Remarkably, an analytical form of the scattering coefficients of equation (6) can be found beyond the Andreev approximation in the case $Z = 0$—see appendix C for details.

3. Thermoelectric properties of the N-S AB ring

Thermoelectricity—i.e. the ability to convert a heat current into an electrical current (Seebeck effect), or vice versa (Peltier effect) – requires an energy asymmetry between electron-like and hole-like quasiparticles, see reference [34] for a pedagogical review. The Seebeck coefficient S assesses the thermovoltage $\Delta V_{\rm th}$ developed by the device in response to a temperature bias at zero charge current, hence expressed in units of $[\mathrm{V\,K^{-1}}]$:

$$S = \left.\frac{\Delta V_{\rm th}}{\Delta T}\right|_{I_{\rm N}=0}. \tag{7}$$

In a N-S two terminal device within the Andreev approximation, the wave vector amplitudes for electrons and holes are both evaluated at the Fermi energy, $k_{\rm e/h} \simeq k_{\rm F}$, preventing any possible electron–hole asymmetry in the transmission probability. This results in the absence of any thermoelectric effects. Beyond the Andreev approximation, there exists an electron–hole asymmetry in the wave vectors, which should lead to a thermoelectric response of the N-S junction. To the best of our knowledge, this has not yet been shown in earlier works, and we take the opportunity of this work to fill this gap[3]. In contrast to the N-S junction, the AB ring hosts quantum interferences that favor thermoelectric effects [27, 28, 42–45].

We show below that the combination of the AB ring and the N-S junction become beneficial to each other, and allow a thermoelectric response of the order of thousands $\mu\mathrm{V\,K^{-1}}$. We investigate the thermoelectric response of the device both in the linear and non-linear response regimes, within and beyond the Andreev approximation.

3.1. Thermoelectric linear response

The linear response regime is defined when $\Delta T = T_{\rm N} - T_{\rm S} \ll T \equiv (T_{\rm N} + T_{\rm S})/2$ for the temperature bias and $e\Delta V = (\mu_{\rm N} - \mu_{\rm S}) \ll k_{\rm B}T$ for the voltage bias [34]. In this situation, the electrical charge current ($I_{\rm N}$) and the heat current ($J_{\rm N}$) in equation (1) are simply expressed in terms of the Onsager matrix $\mathbf{L}$ [34]:

$$\begin{pmatrix} I_{\rm N} \\ J_{\rm N} \end{pmatrix} = \begin{pmatrix} L_{11} & L_{12} \\ L_{21} & L_{22} \end{pmatrix} \begin{pmatrix} \Delta V/T \\ \Delta T/T^2 \end{pmatrix}. \tag{8}$$

The diagonal Onsager coefficients determine the electrical (L_{11}) and heat (L_{22}) conductance, whereas the off-diagonal terms (L_{12}, L_{21}) set the thermoelectric properties of the device in the linear response regime. Let us note that in this two-terminal device, micro-reversibility ensures the transmission function of the AB ring to be an even function of the magnetic flux, hence $L_{12} = L_{21}$ despite the presence of a finite magnetic field [30, 46, 47].

3.1.1. Seebeck coefficient

In the linear response regime, the Seebeck coefficient defined in equation (7) is determined by the Onsager coefficients [34]:

$$S = \frac{1}{T}\frac{L_{12}}{L_{11}}. \tag{9}$$

Figure 2 shows the Seebeck coefficient of the N-S AB ring in the linear response regime within and beyond the Andreev approximation, and compares it to the Seebeck coefficient for the N-S junction alone, without the AB ring. The Seebeck coefficient is plotted as a function of the temperature $T/T_{\rm C}$ for different values of Z. Other parameters have been optimized using the method of the gradient descent in order to get the highest value of the Seebeck coefficient in the temperature range $T/T_{\rm C} \in [0, 2]$. To account for the

[3] We report the recent work [41] in which authors discuss thermoelectric response beyond Andreev approximation up to the first order in $\epsilon/\epsilon_{\rm F}$. In our work we retained all the orders in $\epsilon/\epsilon_{\rm F}$.

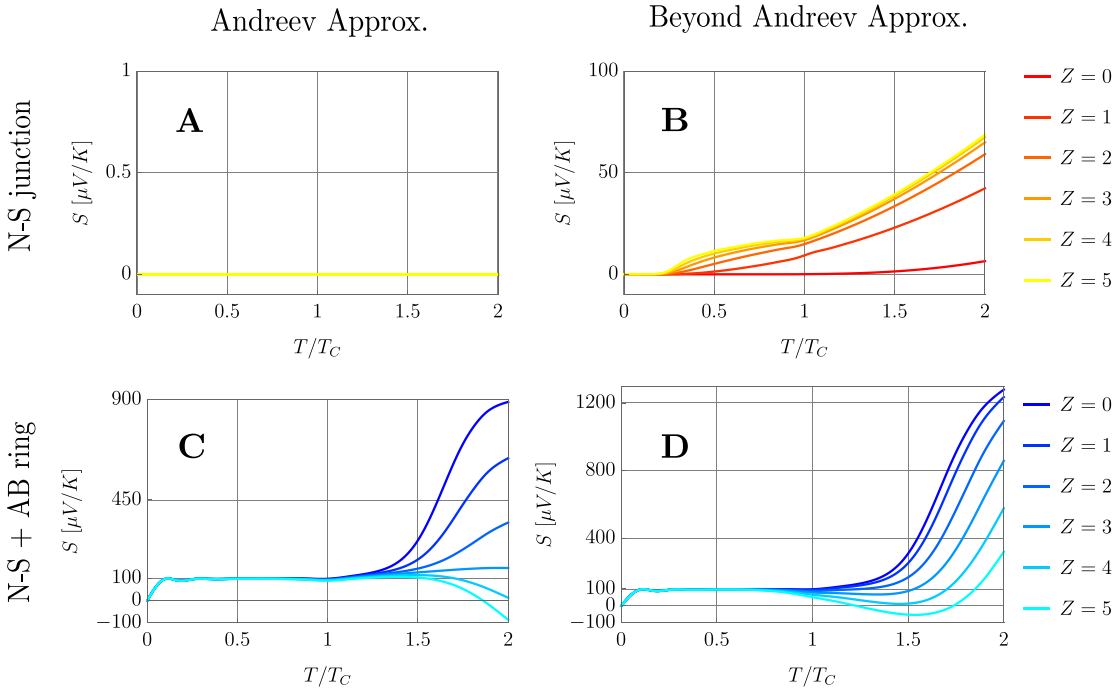

Figure 2. Seebeck coefficient (in units of μV K^{-1}) as a function of the mean temperature T (in units of the critical temperature T_C) for different values of the barrier strength Z. Upper panels show the case of the N-S junction *without* the AB ring, bottom panels show the configuration of the N-S junction *with* the AB ring. Left panels have been obtained in the Andreev approximation ($\epsilon, \Delta \ll \epsilon_F$), right panels have been obtained beyond the Andreev approximation limit with $\epsilon_F = 5\Delta$. Here we considered $k_F\xi = 1$ (where $\xi = \hbar v_F/\Delta$ is the superconducting coherence length), $\tau = 0.5$, while other parameters have been optimized in the temperature range $T/T_C \in [0, 2]$ and are: $L_u/\xi = L_\ell/\xi = 0.1$, $eV_g/\pi\Delta = 0$ and $2\pi\Phi/\Phi_0 = 0.5$.

temperature dependence of the superconducting order parameter, we use the following relation for the energy gap:

$$\Delta(T) = \Delta(0)\tanh\left(1.74\sqrt{\frac{T_C}{T} - 1}\right) \tag{10}$$

which is accurate better than 2% with respect to the self-consistent BCS result [48, 49]. Panel **A** evidences the absence of any thermoelectric response of the N-S junction within the Andreev approximation with $S = 0$ for all values of Z (as explained earlier, in this limit no electron–hole asymmetry exists). Beyond the Andreev approximation, the situation clearly differs, see panel **B**. The Seebeck coefficient is finite and increases monotonically both as a function of temperature and Z reaching values of the order of $\sim$60 μV K^{-1}. Interestingly, it decreases when going to the limit of a transparent barrier, $Z \to 0$. To understand this dependence, we investigated numerically the case $Z = 0$. In this limit, the scattering amplitudes in S_{NS} obtained beyond the Andreev approximation weakly deviate from that given in the Andreev approximation only for $\epsilon \gtrsim \Delta$ within few $k_B T$. As a consequence, at low temperatures the thermoelectric response is weak, and increases by increasing temperature (see red curve in panel **B**).

In panels **C** and **D**, we first observe a plateau, the Seebeck coefficient remains constant at $\sim$100 μV K^{-1}, when the gap is open, i.e. for $T < T_C$. Interestingly, this plateau is independent of the value of Z. At $T \approx T_C$ (when the gap is closed), the Seebeck coefficient starts to deviate until it reaches (at $T = 2T_C$) values of the order of $\sim$900 μV K^{-1} in the Andreev approximation (panel **C**) and $\sim$1300 μV K^{-1} beyond the Andreev approximation (panel **D**). Let us remark that the behavior of the Seebeck coefficient as a function of Z in the presence of the AB ring is not universal, it rather depends on the specific choice of the parameters. In particular, as seen in panels **C** and **D**, the Seebeck coefficient in presence of the AB ring is larger for small Z, while it decreases by increasing Z. This has been obtained by fixing the value of the external magnetic flux at $2\pi\Phi/\Phi_0 = 0.5$. If one would set for instance $2\pi\Phi/\Phi_0 = 0$, the opposite behavior could be observed as verified numerically.

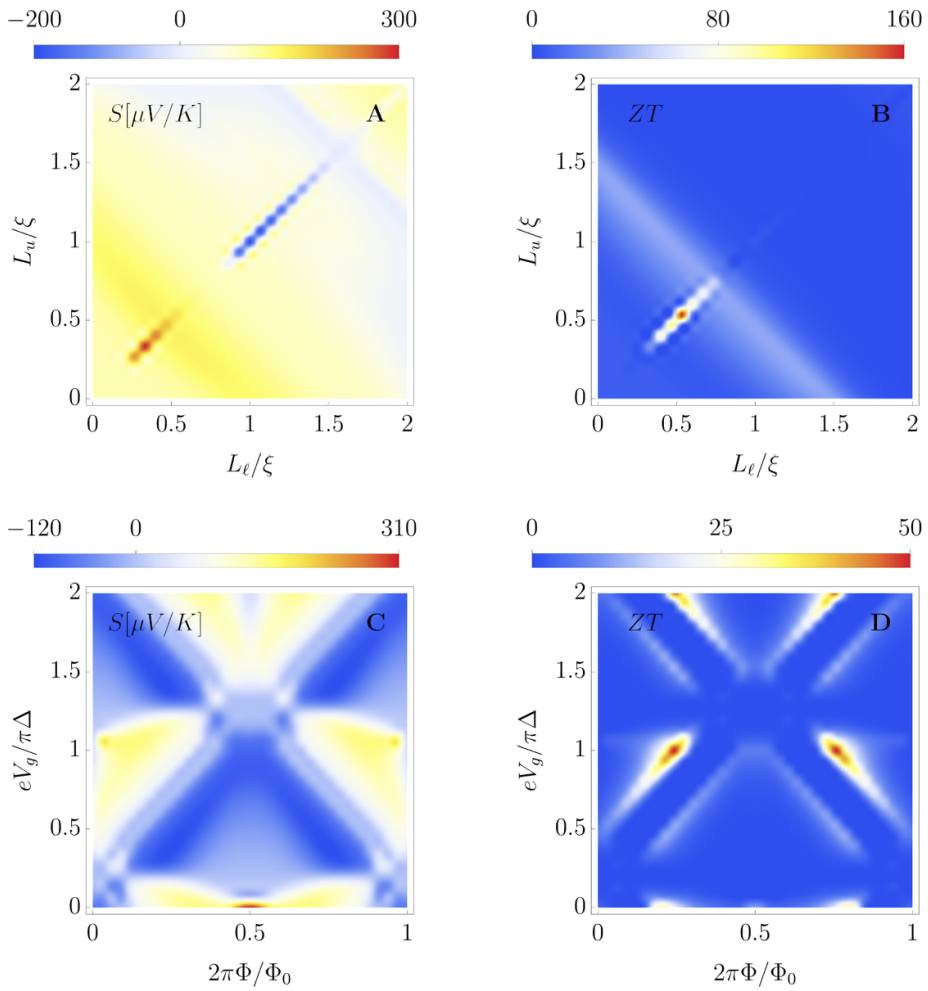

Figure 3. Seebeck coefficient (left panels) in units of μV K^{-1} and the figure of merit ZT (right panels) as function of the upper and lower branches lengths L_u/ξ and L_ℓ/ξ of the AB ring expressed in units of the coherence length $\xi = \hbar v_F/\Delta$ (upper panels) and as a functions of magnetic flux $2\pi\Phi/\Phi_0$ and the gate potential $eV_g/\pi\Delta$ (bottom panels). For upper panels we fixed $eV_g/\pi\Delta = 0$ and $2\pi\Phi/\Phi_0 = 0.5$, for bottom panels we considered $L_u/\xi = L_\ell/\xi = 0.3$: these choices maximize the value of the Seebeck coefficients. All panels plots have been obtained in the Andreev approximation where we considered $\tau = 0.1$, $Z = 0.1$ and $k_F\xi = 1$.

3.1.2. Tunable thermoelectric properties

We now characterize the thermoelectric response and the efficiency of this N-S AB ring as a function of key parameters for an experiment: external gate voltage V_g applied onto one of the arms of the AB ring, length imbalance $\Delta L = L_u - L_\ell$ between the two arms and the AB flux Φ due to an external magnetic field applied perpendicularly to the sample. Panels **A** and **C** of figure 3 show density plots of the Seebeck coefficient as a function of these parameters. Let us remind the reader that the Seebeck coefficient can take both positive and negative values, reflecting electron-like or hole-like dominant behavior [34]. In the N-S AB ring device, it seems advantageous for increasing S to operate with a balanced AB ring, with symmetric arms $L_u = L_\ell$. In this situation, the behavior of S as a function of external gate voltage V_g and AB flux Φ highlights some optimal values to reach high value for S, about 300 μV K^{-1}. Here we have considered a mean temperature $T/T_C = 0.5$ such that the gap of the superconducting lead is open, and a transmission probability for the T-junctions $\tau = 0.1$. The other parameters have been optimized by using the method of the gradient descent in order to get the higher value of the Seebeck coefficient. The right column (panels **B** and **D**) shows the ZT coefficient, a figure of merit for assessing the maximal efficiency η_{max} of a thermoelectric device in the linear response regime. It approaches the Carnot efficiency $\eta_C = \Delta T/T$ for $ZT \to \infty$ [34]. In terms of the Onsager matrix and coefficients introduced in equation (8), it reads:

$$\eta_{max} = \eta_C \frac{\sqrt{ZT+1}-1}{\sqrt{ZT+1}+1} \quad \text{with} \quad ZT = \frac{L_{12}^2}{\mathrm{Det}[\mathbf{L}]}. \tag{11}$$

As it emerges from the top panels of figure 3, both the Seebeck coefficient and the ZT figure of merit are sizable only when the lengths of the upper and lower branches of the AB ring are equal $L_u = L_\ell$,

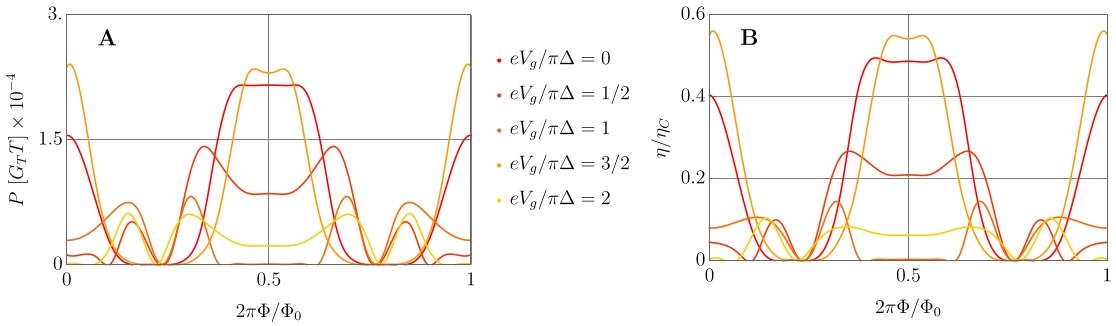

Figure 4. Power in units of $G_T T$, with $G_T = (\pi^2/3h)k_B^2 T$ the thermal conductance quantum (panel **A**), and the efficiency η in units of the Carnot efficiency $\eta_C = \Delta T/T$ (panel **B**) as function of the magnetic flux Φ in units of the flux quantum Φ_0 for different values of the gate voltage $eV_g/\pi\Delta$. Here the other parameters used to maximize the efficiency are: $R_L/(h/2e^2) = 100$, $Z = 0.04$, $\tau = 0.24$, $L_u/\xi = 0.1$, $L_\ell/\xi = 1.26$, $T/T_C = 0.5$ and $\Delta T/T_C = 0.1$.

corresponding to the darker stripe on the diagonal of the density plots. More precisely, the Seebeck coefficient takes its maximal value when $L_u = L_\ell \approx 0.3$, in which case $S \approx 300\ \mu\text{V K}^{-1}$ and $ZT \approx 100$, the latter being one order of magnitude bigger than the one found in reference [27]. This excellent thermoelectric response in the linear regime motivates the investigation of its thermoelectric properties in the non-linear regime. As direct application, we exploit them to propose the N-S AB ring as efficient quantum heat engine in the following section.

3.2. Quantum heat engine in the non-linear response regime

Predicting a high Seebeck coefficient for a given nanoscale device is extremely relevant for designing efficient quantum thermal engines. Indeed, by closing the circuit with a load resistance R_L (see figure 1 (a)) connected with superconducting wires to the device (no Joule dissipation in the wires), one can generate an electrical power P from the thermovoltage developed by the device in response to the thermal bias, $P = \frac{\Delta V_{\text{th}}^2}{R_L}$. The efficiency of such a device is then the ratio of the electrical power (output) over the heat current from the hot contact in the stationary state evaluated at the thermovoltage (input), $\eta = \frac{P}{J_N(\Delta V_{\text{th}})}$.

In the non-linear regime, the thermovoltage developed by the device has to be calculated by solving the following equation for the closed circuit (we refer to [28] and references therein for more details):

$$I_N(\Delta V_{\text{th}}) = -\frac{\Delta V_{\text{th}}}{R_L}. \tag{12}$$

We evaluate numerically the thermovoltage in the closed circuit configuration as a function of the magnetic flux Φ and of the gate voltage V_g, showing the results in figure 4. Panel **A** corresponds to the generated power P and panel **B** to the efficiency η. We predict values for the efficiency up to ∼55% of the Carnot efficiency. Compared to the values η ∼40% obtained with a normal AB structure [28], we can associate the higher efficiency to the N-S interface as it leads to a decrease of the heat current entering the denominator of η. Indeed, the N-S junction acts as a mirror for the heat current: Andreev reflections block energy and heat fluxes since the latter are propagated by single quasi-particles and not by Cooper pairs in the condensate [34]. We note that power and efficiency present the same behavior (in particular reach the maximum for same values of the parameters) as a function of $2\pi\Phi/\Phi_0$, V_g and τ, the transmission of the T-junctions. For the latter dependence on τ, we observe that power and efficiency both reach a maximum value for relatively small values of τ, decrease for τ close to 1, and vanish for $\tau = 0$. These features originate in the AB ring exhibiting a Fabry-Pérot like behavior for small τ (first discussed in [27]). In contrast, $\tau = 0$ corresponds to a fully decoupled ring from the contacts (no transport) and $\tau = 1$ does not contribute to an enhancement of constructive single-particle interferences.

4. Hybrid AB ring as quantum thermal rectifier

Demonstrating thermal rectification with high efficiency at the quantum scale is currently a very active research direction, both from a fundamental point of view and in applied physics for quantum engineering. In a two-terminal setup subject to thermal bias, thermal rectification is achieved when left-to-right currents differ upon exchanging the temperatures of the two contacts. From the theory of superconductivity, it is clear that an efficient way to break left-right symmetry is to exploit the dependence of the DOSs of superconductors as a function of temperature. Indeed, as recalled in equation (10), the superconducting gap,

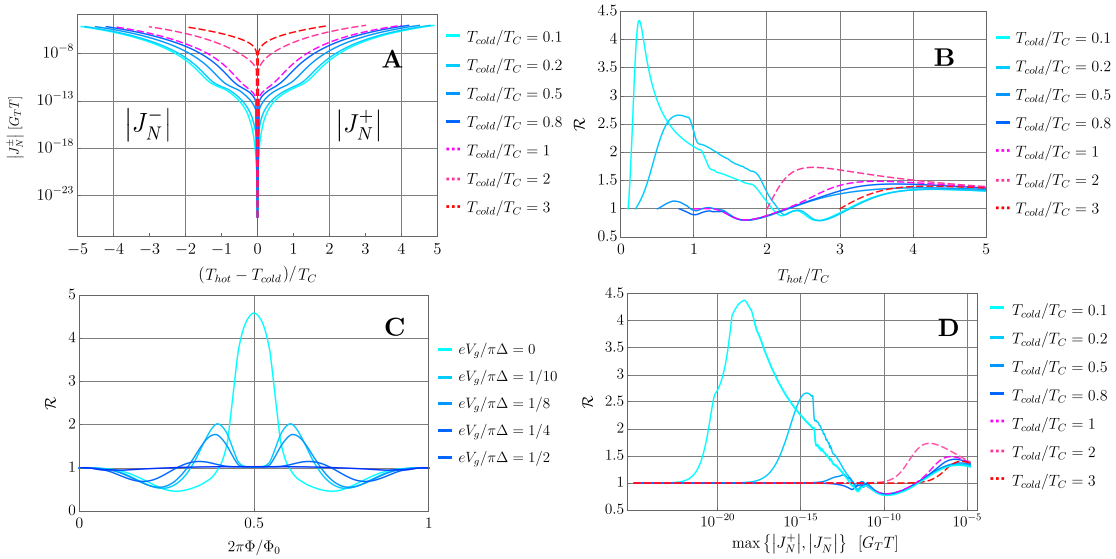

Figure 5. Rectification with the hybrid AB ring. Panel **A**: Log-scale plot of the absolute value of the heat current $|J_N^{\pm}|$ in units of $G_T T$ as a function of $(T_{hot} - T_{cold})/T_C$. Right branch corresponds to $|J_N^+|$ in the forward configuration while left branch represents $|J_N^-|$ in the reverse configuration. Blueish solid curves represent the case in which $T_{cold}/T_C < 1$ (the gap is open in the S contact), reddish dashed curves have been obtained for $T_{cold}/T_C \geqslant 1$ (both contacts behave as normal metals). Panel **B**: Rectification factor $\mathcal{R}$ as function of T_{hot}/T_C for different values of T_{cold}/T_C with $V_g = 0$ and $2\pi\Phi/\Phi_0 = 0.5$. Panel **C** : Rectification factor $\mathcal{R}$ as function of $2\pi\Phi/\Phi_0$ for different values of $eV_g/\pi\Delta$ at fixed values of $T_{cold}/T_C = 0.1$ and $T_{hot}/T_C = 0.15$. Panel **D** : parametric plot of $\mathcal{R}$ and $\max\left\{|J_N^+|, |J_N^-|\right\}$ as a function of T_{hot}/T_C for different values of T_{cold}/T_C. Fixed parameters: $\tau = 0.1$, $Z = 0.2$, $k_F\xi = 1$, $L_u = L_\ell = 0.1$.

and consequently the DOS, changes with temperature [50–53]. Upon exchanging the temperatures, DOS of the contacts are modified, inducing different heat currents in the two configurations. Hence, thermal rectification at the nanoscale was predicted and measured in N-S junctions in the past decade [1].

To investigate and characterize this operating mode for the hybrid N-S AB ring device, we consider again the open-circuit setup (i.e. without the load resistance) beyond the linear response regime. Specifically, we consider two configurations for the thermal bias. In the *forward* configuration, a thermal gradient is created by setting $T_N = T_{hot} > T_S = T_{cold}$, leading to a total heat current J_N^+ flowing from N to S. In the *reverse* thermal bias configuration, the thermal gradient is inverted, $T_N = T_{cold} < T_S = T_{hot}$, leading to a heat current J_N^- flowing from S to N. It follows that thermal rectification is achieved whenever $|J_N^+| \neq |J_N^-|$. Let us remark that the thermovoltage developed by the N-S AB ring in response to a temperature gradient *must* be taken into account when calculating the heat currents J_N^+ and J_N^-. The thermovoltages in the two configurations are solutions of the following equations for the charge current:

$$\begin{cases} I_N\left(\Delta V_{th}^+, T_N = T_{hot}, T_S = T_{cold}\right) = 0 \\ I_N\left(\Delta V_{th}^-, T_N = T_{cold}, T_S = T_{hot}\right) = 0 \end{cases} \tag{13}$$

with the charge current given by equation (1).

Panel **A** in figure 5 shows in log-scale the absolute value of the heat currents $|J_N^{\pm}|$ as a function of $(T_{hot} - T_{cold})/T_C$ for different values of T_{cold}. Note that for $T_{cold}/T_C < 1$ (see blueish solid curves), we probe the superconducting properties of the S contact, while for $T_{cold}/T_C \geqslant 1$ (see reddish dashed curves) both contacts behave as normal metals. Rectification can be assessed by its figure of merit, the rectification factor defined as:

$$\mathcal{R} = |J_N^+| / |J_N^-| . \tag{14}$$

If $\mathcal{R} > 1$, the heat current flows from left to right ($N \to S$), while if $\mathcal{R} < 1$ the heat current flows from right to left ($N \leftarrow S$). If $\mathcal{R} = 1$, the heat current does not have a specific direction, i.e. there is no rectification. Panel **B** in figure 5 represents the rectification factor $\mathcal{R}$ as function of T_{hot}/T_C for different values of T_{cold}/T_C. Here we considered the hot temperature in the range $T_{cold} \leqslant T_{hot} \leqslant 5T_C$, while for larger temperatures, i.e. $T_{hot} \gg T_C$, we verified that $\mathcal{R}$ approaches 1. As can be noticed in panel **B**, the higher rectification occurs for small values of $T_{cold} \ll T_C$, while it decreases by increasing T_{cold}. In particular, a value for rectification of

about $\mathcal{R} \simeq 4.5$ is achieved for $T_{\rm cold}/T_{\rm C} = 0.1$ and $T_{\rm hot}/T_{\rm C} = 0.15$: this corresponds to a value of the forward heat current ($J_{\rm N}^{+}$) greater than 350% compared to the reverse one ($J_{\rm N}^{-}$). Furthermore, it is important to notice that, differently from systems that do not exhibit thermoelectric properties, in our case rectification occurs even for $T_{\rm cold} > T_{\rm C}$, namely when the gap of the superconductor is closed and the system behaves as an effective *N-AB-N* device. This happens because, although in such an effective *N-AB-N* regime the system is left-right symmetric (namely the scattering matrix $\mathcal{S}$ is not affected by the exchange of temperatures, $T_{\rm cold} \leftrightarrow T_{\rm hot}$), the thermovoltage generated in the forward configuration is different from that obtained in the reverse one, i.e. $\Delta V_{\rm th}^{+} \neq \Delta V_{\rm th}^{-}$, as results by explicitly solving equations (13)—see appendix D for more details. This results in a forward heat current different from the reverse one, $\left|J_{\rm N}^{+}(\Delta V_{\rm th}^{+})\right| \neq \left|J_{\rm N}^{-}(\Delta V_{\rm th}^{-})\right|$, which reflects into a finite rectification. However, it is important to stress that the rectification obtained when the system behaves like an effective *N-AB-N* device (i.e. when $T_{\rm cold} > T_{\rm C}$) is at least 3 times smaller than the one obtained when the gap is open and the right lead is still superconducting (i.e. when $T_{\rm cold} < T_{\rm C}$), as can be seen by comparing the cyan solid curve with the violet dashed one in panel **B** of figure 5.

We also investigate the tunability of this rectifier by means of the external parameters provided by the N-S AB ring device. Panel **C** in figure 5 shows $\mathcal{R}$ as a function of the magnetic flux Φ for different values of the gate voltage $V_{\rm g}$. The temperatures $T_{\rm cold}/T_{\rm C} = 0.1$ and $T_{\rm hot}/T_{\rm C} = 0.15$ have been fixed to optimize $\mathcal{R}$. It becomes clear that this device is fully phase-tunable. Controlling the magnetic flux Φ allows us to turn on and off the rectification ability of the N-S AB ring.

Finally, we would like to emphasize that a quantum heat rectifier should also be characterized by good heat conduction properties to constitute a useful device. Indeed, as recently discussed in [54], there typically exits a trade-off between heat rectification and heat conduction. Large rectification factors often occur at low maximum heat current through the device. This motivates us to investigate the heat rectification factor and the heat currents in a complementary way. We show in panel **D** a parametric plot of $\mathcal{R}$ and $\max\left\{\left|J_{\rm N}^{+}\right|, \left|J_{\rm N}^{-}\right|\right\}$ as a function of $T_{\rm hot}/T_{\rm C}$. While the trade-off between heat rectification and heat conduction is clearly visible (highest $\mathcal{R}$ occurs at lowest $\max\left\{\left|J_{\rm N}^{+}\right|, \left|J_{\rm N}^{-}\right|\right\}$, see cyan solid curve corresponding to $T_{\rm cold}/T_{\rm C} = 0.1$), the numerical results predict sizable rectification of 50% happening at several tens of $[nW]$ for all values of $T_{\rm cold}$.

5. Experimental implementation of the hybrid AB ring

Let us now discuss a possible experimental setup to implement the hybrid AB interferometer. Since the structure also contains a superconducting lead, III–V semiconducting alloys like InAs [55–58] or $In_{0.80}Ga_{0.20}As$ [59, 60] two-dimensional electron gases (2DEGs) are suitable candidates for the realization of the ballistic loop structure. These materials typically provide Schottky barrier-free contacts with metals, which is a crucial requirement in order to achieve highly-transparent N-S interfaces, and thereby maximize Andreev reflection at the contact with the superconductor. Such III–V 2DEGs can be easily gated by means of side or top gates in order to finely tailor the details of the thermoelectric AB structure. As far as the superconducting element is concerned, aluminum (Al, providing an energy gap of $\sim$200 μeV and critical temperature around 1.4 K) or niobium (Nb, providing an energy gap of $\sim$1.5 meV and critical temperature $\sim$9 K) thin layers are ideal superconductors to be coupled to the 2DEG AB ring.

The AB quantum thermal structure analyzed so far needs to be thermally-biased in order to provide either thermoelectric response or heat rectification properties [1]. To this end superconducting tunnel junctions (typically made of oxidized Al layers) can be integrated in the normal and superconducting leads forming the structure [3], and can be used as electron heaters to impose a suitable thermal gradient across the structure via Joule heating, or can be used to measure the quasiparticle temperature thereby operating as sensitive electron thermometers [3]. On the one hand, the thermoelectric response of the hybrid AB interferometer can be proved by setting a thermal gradient across the ring (from a few tens to a few hundreds mK depending on the average temperature of the structure), and by measuring either the thermovoltage in an open-circuit configuration or the thermocurrent by closing the circuit upon a suitable loading resistor [1]. On the other hand, the heat rectification character of the system can be demonstrated by tunnel-coupling two identical normal metal (N) reservoirs to the N-S AB structure [11, 61], one on the left and the other on the right, each of them equipped with superconducting tunnel junctions thereby implementing electron heaters and thermometers. The forward thermal bias configuration can be achieved by intentionally increasing the electronic temperature up to $T_{\rm hot}$ in one of the two N electrodes (i.e. up to several hundreds mK to achieve the full non-linear regime in temperature), and by measuring the resulting steady-state temperature in the opposite electrode. The reverse thermal bias configuration is obtained similarly by simply inverting the heating in the other N electrode. The difference of the two measured temperatures for any given $T_{\rm hot}$ can be used to assess the degree of thermal rectification as a function of electrostatic gating and magnetic flux [1, 11].

6. Conclusions

In summary, we have theoretically analyzed both the thermoelectric and rectification response of a ballistic interferometer consisting of an AB quantum ring coupled to a normal metal and a superconducting lead. As a thermoelectric quantum device, the N-S AB interferometer is able to provide a sizable Seebeck coefficient as large as 100 μV K^{-1} below the superconducting critical temperature T_C, independently of the transmissivity of the ring/superconductor interface. In addition, at temperatures larger than T_C (when the superconducting lead is in the metallic regime), the Seeebeck coefficient obtains values exceeding 1 mV K^{-1} for an ideal contact with the superconductor, whereas it is strongly suppressed by decreasing the ring/superconductor interface transmissivity. Yet, in terms of the ZT coefficient, the N-S AB device obtains values as large as $\sim$160, which appears promising in light of the implementation of efficient quantum heat engines. In such a context, sizable values as large as $\sim$55% of the Carnot efficiency can, in principle, be achieved in the structure under suitable tuning of the gate voltage and the magnetic flux piercing the interferometer. All this confirms the potential of the N-S AB interferometer as a prototypical platform for the realization of efficient quantum thermal machines.

Moreover, the presence of a superconducting lead breaks left-right thermal symmetry in the structure, thereby allowing finite heat rectification to occur in the interferometer. In particular, rectification coefficients as large as $\sim$350% can be achieved upon proper tuning of the structure parameters.

Finally, as far as the realization of the structure is concerned, III–V semiconducting alloys such as InAs or $In_{0.80}Ga_{0.20}As$ realizing two-dimensional electron gases combined to an Al or Nb superconducting electrode are suitable candidates for the realization of the ballistic AB hybrid interferometer. The flexibility offered by the above material systems seems indeed ideal in light of the realization of quantum thermoelectric machines implemented through ballistic AB interferometers to be exploited in future quantum technology applications operating at subkelvin temperatures.

Data availability statement

All data that support the findings of this study are included within the article (and any supplementary files).

Acknowledgment

F G acknowledges the EU's Horizon 2020 research and innovation program under Grant Agreement No. 800923 (SUPERTED) and No. 964398 (SUPERGATE) for partial financial support. G B and G H acknowledge support from the Swiss National Science Foundation through the NCCR QSIT (GB and GH) and from the NCCR SwissMAP and a starting grant PRIMA PR00P2_179748 (GH).

Appendix A. Scattering matrix of the AB ring

Here we provide details on the derivation of the scattering matrix S_{AB} of equation (4). Specifically, in appendix A.1, we proceed by writing first the particle-scattering matrices S_{T_1,T_2} for the T-junctions and S_R for the ring. Then, in appendix A.2, we combine them to get the 2×2 particle-scattering matrix of the AB ring connected with the T-junctions, that only describes the scattering processes of particles. Finally, in order to account for the presence of holes, in appendix A.3 we use the BdG formalism to extend the matrix to the full particle-hole space.

A.1. T-junctions and AB ring particle-scattering matrices

As shown in figure A1, we model our setup as a two-terminal geometry consisting of a AB ring connected to two reservoirs through T-junctions [30]. This system can be described via three scattering matrices: S_{T_1} and S_{T_2} describing respectively the left and right T-junctions connecting the AB ring to the contacts, and S_R which describes the ring. Following [27, 28, 30], the real particle-scattering matrices of the left and right T-junctions are given by

$$\begin{pmatrix} c_1^- \\ c_{R1}^{u+} \\ c_{R1}^{\ell+} \end{pmatrix} = \begin{pmatrix} -(a_1+b_1) & \sqrt{\tau_1/2} & \sqrt{\tau_1/2} \\ \sqrt{\tau_1/2} & a_1 & b_1 \\ \sqrt{\tau_1/2} & b_1 & a_1 \end{pmatrix}_{S_{T_1}} \begin{pmatrix} c_1^+ \\ c_{R1}^{u-} \\ c_{R1}^{\ell-} \end{pmatrix} \tag{A.1}$$

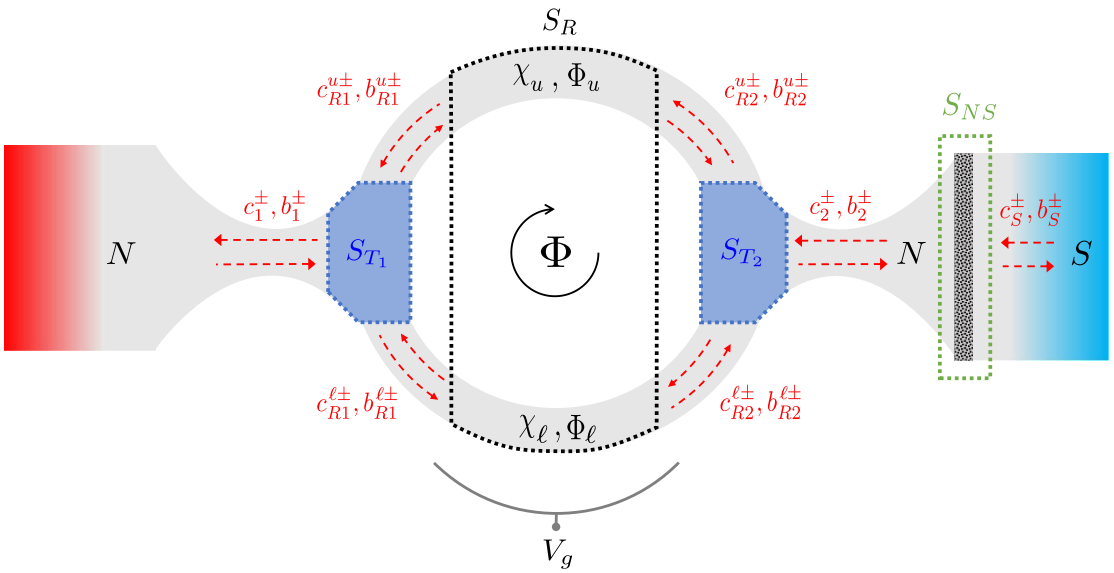

Figure A1. Sketch of the hybrid AB ring. Dotted lines with different colors encircle respectively the scattering regions of the T-junctions (blue dotted lines), the ring (black dotted line) and the N-S junction (green dotted line). Red dashed arrows indicate the direction of propagation of the incoming and outgoing particles (holes).

$$\begin{pmatrix} c^{u-}_{R2} \\ c^{\ell-}_{R2} \\ c^{+}_{2} \end{pmatrix} = \begin{pmatrix} a_2 & b_2 & \sqrt{\tau_2/2} \\ b_2 & a_2 & \sqrt{\tau_2/2} \\ \sqrt{\tau_2/2} & \sqrt{\tau_2/2} & -(a_2+b_2) \end{pmatrix}_{S_{T_2}} \begin{pmatrix} c^{u+}_{R2} \\ c^{\ell+}_{R2} \\ c^{-}_{2} \end{pmatrix} \tag{A.2}$$

where we indicated with $c^{\pm}_i$ the incoming and outgoing particles in the left ($i=1$) and right ($i=2$) lead respectively, and with $c^{k\pm}_{Rj}$ the incoming and outgoing particles on the left ($j=R1$) and right ($j=R2$) side of the ring. The index $k=u,\ell$ labels, respectively, the upper and lower branch of the ring, and $\pm$ indicate the direction of propagation of particles ($+$ for right movers and $-$ for left movers). In equations (A.1) and (A.2), we defined the scattering amplitudes

$$\begin{aligned} a_i &= \frac{1}{2}\left(\sqrt{1-\tau_i}-1\right) \\ b_i &= \frac{1}{2}\left(\sqrt{1-\tau_i}+1\right) \end{aligned} \tag{A.3}$$

where $\tau_i \in [0,1]$ represents the transmission probability of the left ($i=1$) and right ($i=2$) T-junction respectively. For simplicity, in the main text we considered $\tau=\tau_1=\tau_2$ (symmetric T-junctions). As a further remark, it is useful to notice that, with the choice of basis we did in equations (A.1) and (A.2), the scattering matrices of the T-junctions can be written in the standard form

$$S_{T_i} = \begin{pmatrix} r_i & t'_i \\ t_i & r'_i \end{pmatrix}, \tag{A.4}$$

where r_i and r'_i are square block matrices concerning reflected particles, whereas t_i and t'_i are rectangular block matrices concerning particles transmitted through the left ($i=1$) and right ($i=2$) T-junction respectively. In the same way we can write the particle-scattering matrix S_R describing the ring, which is given by

$$\begin{pmatrix} c^{u-}_{R1} \\ c^{\ell-}_{R1} \\ c^{u+}_{R2} \\ c^{\ell+}_{R2} \end{pmatrix} = \begin{pmatrix} 0 & 0 & e^{i(\chi_u-\Phi_u)} & 0 \\ 0 & 0 & 0 & e^{i(\chi_\ell-\Phi_\ell)} \\ e^{i(\Phi_u+\chi_u)} & 0 & 0 & 0 \\ 0 & e^{i(\Phi_\ell+\chi_\ell)} & 0 & 0 \end{pmatrix}_{S_R} \begin{pmatrix} c^{u+}_{R1} \\ c^{\ell+}_{R1} \\ c^{u-}_{R2} \\ c^{\ell-}_{R2} \end{pmatrix} \tag{A.5}$$

where χ_i are the dynamical phases that electrons acquire while traveling in each arm $i=u,\ell$. Moreover, the application of the magnetic flux Φ across the AB ring causes the particles to acquire additional phases on each arm (namely, Φ_u in the upper and Φ_ℓ in the lower arm), such that $\Phi_u-\Phi_\ell=2\pi\Phi/\Phi_0$ with $\Phi_0=h/e$

being the flux quantum. As a result, right moving particles propagating in each arm ($i = u, \ell$) acquire a global dynamical phase $\chi_i + \Phi_i$, while left moving particle get a global phase $\chi_i - \Phi_i$. Also in this case S_R can be written in the form

$$S_R = \begin{pmatrix} r_R & t'_R \\ t_R & r'_R \end{pmatrix}. \tag{A.6}$$

As shown in [27, 28], by linearizing the spectrum around the Fermi energy ϵ_F and taking into account an additional voltage gate V_g applied to the lower arm of the ring, we can write the dynamical phases χ_u and χ_ℓ in the following way

$$\chi_u = \left[k_F + \frac{\epsilon - \epsilon_F}{\hbar v_F}\right] L_u \equiv \left[\frac{\xi}{\lambda_F} + \frac{\epsilon - \epsilon_F}{\Delta}\right] \frac{L_u}{\xi} \tag{A.7}$$

$$\chi_\ell = \left[k_F + \frac{\epsilon - (\epsilon_F + V_g)}{\hbar v_F}\right] L_\ell \equiv \left[\frac{\xi}{\lambda_F} + \frac{\epsilon - (\epsilon_F + V_g)}{\Delta}\right] \frac{L_\ell}{\xi} \tag{A.8}$$

with L_u and L_ℓ the lengths of the upper and lower arm respectively, and where we introduced the Fermi wave vector $k_F = \sqrt{2m\epsilon_F}/\hbar = 1/\lambda_F$ (with λ_F the Fermi wave length). In equations (A.7) and (A.8), we expressed all the quantities with respect to the superconducting energy gap Δ and the coherence length $\xi = \hbar v_F/\Delta$.

A.2. Combination of the scattering matrices

By following [37, 38] we first combine matrices S_{T_1} of equation (A.1) and S_R of equation (A.5), and obtain

$$S_{T_1} \circ S_R = \begin{pmatrix} r & t' \\ t & r' \end{pmatrix}, \tag{A.9}$$

in which

$$\begin{aligned} r &= r_1 + t'_1 r_R \left[\mathbb{1} - r'_1 r_R\right]^{-1} t_1 \\ r' &= r'_R + t_R \left[\mathbb{1} - r'_1 r_R\right]^{-1} r'_1 t'_R \\ t &= t_R \left[\mathbb{1} - r'_1 r_R\right]^{-1} t_1 \\ t' &= t'_1 \left[\mathbb{1} - r_R r'_1\right]^{-1} t'_R, \end{aligned} \tag{A.10}$$

where $\mathbb{1}$ stands for the 2×2 identity matrix. Finally, by applying the same procedure but adding S_{T_2} we obtain the particle-scattering matrix of the AB ring

$$S^e_{AB} \equiv S_{T_1} \circ S_R \circ S_{T_2} \tag{A.11}$$

which takes the following form

$$\begin{aligned} S^e_{AB} &= \begin{pmatrix} r^{ee}_{AB} & t'^{ee}_{AB} \\ t^{ee}_{AB} & r'^{ee}_{AB} \end{pmatrix} \\ &= \begin{pmatrix} \frac{f_- \cos(\delta\chi) - f_+ \cos(\Phi) + 4\sqrt{1-\tau}\cos(\chi)}{f_\pm \cos(\delta\chi) + f_+ \cos(\Phi) + 2i\tau \sin(\chi) + 2(\tau-2)\cos(\chi)} & \frac{2i\tau e^{-i\Phi/2}\left(\sin(\chi_u) + e^{i\Phi}\sin(\chi_\ell)\right)}{f_- \cos(\delta\chi) + f_+ \cos(\Phi) + 2i\tau \sin(\chi) + 2(\tau-2)\cos(\chi)} \\ \frac{2i\tau e^{-i\Phi/2}\left(\sin(\chi_\ell) + e^{i\Phi}\sin(\chi_u)\right)}{f_- \cos(\delta\chi) + f_+ \cos(\Phi) + 2i\tau \sin(\chi) + 2(\tau-2)\cos(\chi)} & \frac{f_- \cos(\delta\chi) - f_+ \cos(\Phi) + 4\sqrt{1-\tau}\cos(\chi)}{f_- \cos(\delta\chi) + f_+ \cos(\Phi) + 2i\tau \sin(\chi) + 2(\tau-2)\cos(\chi)} \end{pmatrix} \end{aligned} \tag{A.12}$$

in which the upper index e indicates that such scattering matrix only relates incoming with outgoing particles (namely electrons), and where we defined the quantities: $\chi = \chi_u + \chi_\ell$, $\delta\chi = \chi_u - \chi_\ell$, $f_- = (\sqrt{1-\tau} - 1)^2$ and $f_+ = (\sqrt{1-\tau} + 1)^2$. From equation (A.12) we can compute the transmission function which is given by

$$T_{AB} = |t^{ee}_{AB}|^2 = |t'^{ee}_{AB}|^2 = \frac{4\tau^2\left(2\cos(\Phi)\sin(\chi_\ell)\sin(\chi_u) + \sin^2(\chi_\ell) + \sin^2(\chi_u)\right)}{\left[f_- \cos(\delta\chi) + f_+ \cos(\Phi) + 2(\tau-2)\cos(\chi)\right]^2 + 4\tau^2 \sin^2(\chi)}. \tag{A.13}$$

A.3. Extension with the BdG formalism

In order to properly describe the transport in presence of a superconducting component, it is mandatory to take into account for holes. In this respect the particle-scattering matrix S^{e}_{AB} of equation (A.12), can be extended in the BdG formalism by changing the sign of the energy and taking the complex conjugate as specified by the particle-hole symmetry relations already introduced in equation (5). As a result we obtain the expression of the S_{AB} full scattering matrix as presented in equation (4) of the main text, which we propose here again making explicit the scattering basis:

$$\begin{pmatrix} c_1^- \\ b_1^- \\ c_2^+ \\ b_2^+ \end{pmatrix} = \begin{pmatrix} r^{ee}_{AB}(\epsilon) & 0 & t'^{ee}_{AB}(\epsilon) & 0 \\ 0 & r^{hh}_{AB}(-\epsilon)^* & 0 & t'^{hh}_{AB}(-\epsilon)^* \\ t^{ee}_{AB}(\epsilon) & 0 & r'^{ee}_{AB}(\epsilon) & 0 \\ 0 & t^{hh}_{AB}(-\epsilon)^* & 0 & r'^{hh}_{AB}(-\epsilon)^* \end{pmatrix}_{S_{AB}} \begin{pmatrix} c_1^+ \\ b_1^+ \\ c_2^- \\ b_2^- \end{pmatrix} \tag{A.14}$$

where we indicated with $b_i^{\pm}$ the incoming and outgoing holes in the left ($i=1$) and the right ($i=2$) lead respectively. As already mentioned in the main text, in equation (A.14), each submatrix takes a block-diagonal form since in the ring an electron cannot be converted into a hole or vice versa.

Appendix B. N-S junction scattering matrix

The scattering matrix equation for S_{NS}, describing the N-S interface between the ring and the superconducting lead, can be written as

$$\begin{pmatrix} c_2^- \\ b_2^- \\ c_S^+ \\ b_S^+ \end{pmatrix} = \begin{pmatrix} r_{ee} & r_{eh} & t_{e\tilde{e}} & t_{e\tilde{h}} \\ r_{he} & r_{hh} & t_{h\tilde{e}} & t_{h\tilde{h}} \\ t_{e\tilde{e}} & t_{h\tilde{e}} & r_{\tilde{e}\tilde{e}} & r_{\tilde{e}\tilde{h}} \\ t_{e\tilde{h}} & t_{h\tilde{h}} & r_{\tilde{e}\tilde{h}} & r_{\tilde{h}\tilde{h}} \end{pmatrix}_{S_{NS}} \begin{pmatrix} c_2^+ \\ b_2^+ \\ c_S^- \\ b_S^- \end{pmatrix} \tag{B.1}$$

where we indicate with $c_S^{\pm}/b_S^{\pm}$ the incoming and outgoing quasiparticles/quasiholes in the superconductor, with $\pm$ labeling the direction of propagation of quasiparticles ($+$ for right movers and $-$ for left movers). In equation (B.1), the scattering coefficients have been obtained by solving the wave function matching problem at the interface between the ring and the superconducting contact in the so-called Andreev approximation limit (when $\epsilon, \Delta \ll \epsilon_F$), and take the following form

$$r_{ee} = -\frac{Z(i+Z)\left(u_0^2 - v_0^2\right)}{u_0^2 + Z^2\left(u_0^2 - v_0^2\right)} \tag{B.2a}$$

$$r_{he} = \frac{u_0 v_0}{u_0^2 + Z^2\left(u_0^2 - v_0^2\right)} e^{-i\phi} \tag{B.2b}$$

$$t_{\tilde{e}e} = \frac{(1-iZ)\, u_0 \sqrt{u_0^2 - v_0^2}}{u_0^2 + Z^2\left(u_0^2 - v_0^2\right)} e^{-i\frac{\phi}{2}} \cdot \Theta(\epsilon - \Delta) \tag{B.2c}$$

$$t_{\tilde{h}e} = \frac{Z v_0 \sqrt{u_0^2 - v_0^2}}{u_0^2 + Z^2\left(u_0^2 - v_0^2\right)} e^{-i\frac{\phi}{2}} \cdot \Theta(\epsilon - \Delta) \tag{B.2d}$$

while the remaining scattering coefficients respect the following relations

$$\begin{cases} r_{\tilde{e}\tilde{e}} = r^*_{\tilde{h}\tilde{h}} = r^*_{hh} = r_{ee} \\ -r_{\tilde{h}\tilde{e}} e^{-i\phi} = -r^*_{\tilde{e}h} e^{-i\phi} = r^*_{eh} = r_{he} \\ t_{e\tilde{e}} e^{-i\phi} = t^*_{hh} e^{-i\phi} = t^*_{\tilde{h}h} = t_{\tilde{e}e} \\ -t_{h\tilde{e}} = -t^*_{e\tilde{h}} = t^*_{\tilde{e}h} = t_{\tilde{h}e} \end{cases} . \tag{B.3}$$

As already mentioned in the main text, it is important to notice that, within the Andreev approximation, all the details about the curvature of the eigenspectrum dispersion relations are completely lost. As a consequence, themoelectric effects may result strongly suppressed. Instead, for a better description of the thermoelectric phenomena in hybrid superconducting systems, it is necessary to go beyond the Andreev

approximation (see appendix C for more details). In equations (B.2) we introduced the so-call coherence factors u_0 and v_0 which take the following form

$$u_0(\epsilon) = \sqrt{\frac{1}{2}\left(1+\sqrt{\frac{\epsilon^2-\Delta^2}{\epsilon^2}}\right)} \equiv \sqrt{\frac{\Delta}{2\epsilon}}e^{\frac{1}{2}h(\epsilon)}$$
$$v_0(\epsilon) = \sqrt{\frac{1}{2}\left(1-\sqrt{\frac{\epsilon^2-\Delta^2}{\epsilon^2}}\right)} \equiv \sqrt{\frac{\Delta}{2\epsilon}}e^{-\frac{1}{2}h(\epsilon)} \tag{B.4}$$

with

$$h(\epsilon) \equiv \begin{cases} \text{arcCosh}\left(\frac{\epsilon}{\Delta}\right) & \text{for} \quad \epsilon > \Delta \\ i\arccos\left(\frac{\epsilon}{\Delta}\right) & \text{for} \quad \epsilon < \Delta \end{cases}. \tag{B.5}$$

Moreover, the scattering coefficients of equations (B.2), depend explicitly on the dimensionless transparency parameter Z which characterizes the interface with the superconductor [31].

Appendix C. Beyond the Andreev approximation

Here we present the explicit expressions of the scattering coefficients of equation (6), obtained beyond the Andreev approximation in the case of an ideal interface $Z = 0$:

$$r_{ee} = \frac{e^{2ixk_e}\left(-\Gamma q_{\tilde{e}}q_{\tilde{h}} + \Gamma k_e k_h + \Xi_1 k_e - \Xi_2 k_h\right)}{\Gamma q_{\tilde{e}}q_{\tilde{h}} + \Gamma k_e k_h + \Xi_1 k_e + \Xi_2 k_h} \qquad r_{eh} = \frac{2u_0 v_0\sqrt{k_e k_h}\left(q_{\tilde{e}} + q_{\tilde{h}}\right)e^{i(xk_e - xk_h + \phi)}}{\Gamma q_{\tilde{e}}q_{\tilde{h}} + \Gamma k_e k_h + \Xi_1 k_e + \Xi_2 k_h}$$
$$r_{he} = \frac{2u_0 v_0\sqrt{k_e k_h}\left(q_{\tilde{e}} + q_{\tilde{h}}\right)e^{i(xk_e - xk_h - \phi)}}{\Gamma q_{\tilde{e}}q_{\tilde{h}} + \Gamma k_e k_h + \Xi_1 k_e + \Xi_2 k_h} \qquad r_{hh} = \frac{e^{-2ixk_h}\left(-\Gamma q_{\tilde{e}}q_{\tilde{h}} + \Gamma k_e k_h - \Xi_1 k_e + \Xi_2 k_h\right)}{\Gamma q_{\tilde{e}}q_{\tilde{h}} + \Gamma k_e k_h + \Xi_1 k_e + \Xi_2 k_h}$$
$$t_{\tilde{e}e} = \frac{2u_0\left(q_{\tilde{h}} + k_h\right)\sqrt{\Gamma k_e q_{\tilde{e}}}e^{\frac{1}{2}i(-2xq_{\tilde{e}} + 2xk_e - \phi)}}{\Gamma q_{\tilde{e}}q_{\tilde{h}} + \Gamma k_e k_h + \Xi_1 k_e + \Xi_2 k_h} \qquad t_{\tilde{e}h} = -\frac{2v_0\left(k_e - q_{\tilde{h}}\right)\sqrt{\Gamma k_h q_{\tilde{e}}}e^{-\frac{1}{2}i(2xq_{\tilde{e}} + 2xk_h - \phi)}}{\Gamma q_{\tilde{e}}q_{\tilde{h}} + \Gamma k_e k_h + \Xi_1 k_e + \Xi_2 k_h}$$
$$t_{\tilde{h}e} = -\frac{2v_0\left(k_h - q_{\tilde{e}}\right)\sqrt{\Gamma k_e q_{\tilde{h}}}e^{\frac{1}{2}i(2xq_{\tilde{h}} + 2xk_e - \phi)}}{\Gamma q_{\tilde{e}}q_{\tilde{h}} + \Gamma k_e k_h + \Xi_1 k_e + \Xi_2 k_h} \qquad t_{\tilde{h}h} = \frac{2u_0\left(q_{\tilde{e}} + k_e\right)\sqrt{\Gamma k_h q_{\tilde{h}}}e^{ixq_{\tilde{h}} - ixk_h + \frac{i\phi}{2}}}{\Gamma q_{\tilde{e}}q_{\tilde{h}} + \Gamma k_e k_h + \Xi_1 k_e + \Xi_2 k_h}$$

$$r_{\tilde{e}\tilde{e}} = \frac{e^{-2ixq_{\tilde{e}}}\left(\Gamma q_{\tilde{e}}q_{\tilde{h}} - \Gamma k_e k_h - \Xi_3 k_e + \Xi_4 k_h\right)}{\Gamma q_{\tilde{e}}q_{\tilde{h}} + \Gamma k_e k_h + \Xi_1 k_e + \Xi_2 k_h} \qquad r_{\tilde{e}\tilde{h}} = -\frac{2u_0 v_0\left(k_e + k_h\right)\sqrt{q_{\tilde{e}}q_{\tilde{h}}}e^{-ix\left(q_{\tilde{e}} - q_{\tilde{h}}\right)}}{\Gamma q_{\tilde{e}}q_{\tilde{h}} + \Gamma k_e k_h + \Xi_1 k_e + \Xi_2 k_h}$$
$$r_{\tilde{h}\tilde{e}} = -\frac{2u_0 v_0\left(k_e + k_h\right)\sqrt{q_{\tilde{e}}q_{\tilde{h}}}e^{-ix\left(q_{\tilde{e}} - q_{\tilde{h}}\right)}}{\Gamma q_{\tilde{e}}q_{\tilde{h}} + \Gamma k_e k_h + \Xi_1 k_e + \Xi_2 k_h} \qquad r_{\tilde{h}\tilde{h}} = \frac{e^{2ixq_{\tilde{h}}}\left(\Gamma q_{\tilde{e}}q_{\tilde{h}} - \Gamma k_e k_h + \Xi_3 k_e - \Xi_4 k_h\right)}{\Gamma q_{\tilde{e}}q_{\tilde{h}} + \Gamma k_e k_h + \Xi_1 k_e + \Xi_2 k_h}$$
$$t_{\tilde{e}\tilde{e}} = \frac{2u_0\left(q_{\tilde{h}} + k_h\right)\sqrt{\Gamma k_e q_{\tilde{e}}}e^{\frac{1}{2}i(-2xq_{\tilde{e}} + 2xk_e + \phi)}}{\Gamma q_{\tilde{e}}q_{\tilde{h}} + \Gamma k_e k_h + \Xi_1 k_e + \Xi_2 k_h} \qquad t_{\tilde{e}\tilde{h}} = -\frac{2v_0\left(k_h - q_{\tilde{e}}\right)\sqrt{\Gamma k_e q_{\tilde{h}}}e^{\frac{1}{2}i\left(2xq_{\tilde{h}} + 2xk_e + \phi\right)}}{\Gamma q_{\tilde{e}}q_{\tilde{h}} + \Gamma k_e k_h + \Xi_1 k_e + \Xi_2 k_h}$$
$$t_{\tilde{h}\tilde{e}} = -\frac{2v_0\left(k_e - q_{\tilde{h}}\right)\sqrt{\Gamma k_h q_{\tilde{e}}}e^{-\frac{1}{2}i(2xq_{\tilde{e}} + 2xk_h + \phi)}}{\Gamma q_{\tilde{e}}q_{\tilde{h}} + \Gamma k_e k_h + \Xi_1 k_e + \Xi_2 k_h} \qquad t_{\tilde{h}\tilde{h}} = \frac{2u_0\left(q_{\tilde{e}} + k_e\right)\sqrt{\Gamma k_h q_{\tilde{h}}}e^{-\frac{1}{2}i\left(-2xq_{\tilde{h}} + 2xk_h + \phi\right)}}{\Gamma q_{\tilde{e}}q_{\tilde{h}} + \Gamma k_e k_h + \Xi_1 k_e + \Xi_2 k_h}$$

where we defined the quantities

$$\Gamma = u_0^2 - v_0^2,$$

and

$$\begin{pmatrix}\Xi_1 & \Xi_2 \\ \Xi_3 & \Xi_4\end{pmatrix} = \begin{pmatrix}q_{\tilde{h}} & q_{\tilde{e}} \\ q_{\tilde{h}} & q_{\tilde{e}}\end{pmatrix}u_0^2 + \begin{pmatrix}q_{\tilde{e}} & q_{\tilde{h}} \\ -q_{\tilde{e}} & -q_{\tilde{h}}\end{pmatrix}v_0^2.$$

Above we introduced the electron and hole wave vector amplitudes

$$k_e = k_F\sqrt{1+\frac{\epsilon}{\epsilon_F}}; \qquad k_h = k_F\sqrt{1-\frac{\epsilon}{\epsilon_F}} \tag{C.1}$$

with $k_F = \sqrt{2m\epsilon_F}/\hbar$ the Fermi wave vector, and the wave vector amplitudes

$$q_{\tilde{e}} = k_F\sqrt{1+\sqrt{\frac{\epsilon^2-\Delta^2}{\epsilon_F^2}}}; \qquad q_{\tilde{h}} = k_F\sqrt{1-\sqrt{\frac{\epsilon^2-\Delta^2}{\epsilon_F^2}}} \tag{C.2}$$

for quasiparticles and quasiholes respectively.

Appendix D. Heat rectification beyond T_C

As we mentioned in section 4, although the system is left-right symmetric for $T_{cold} > T_C$, the thermovoltage generated in the forward configuration turns out to be different from that obtained in the reverse one, i.e. $|\Delta V_{th}^{+}| \neq |\Delta V_{th}^{-}|$. This can be understood by explicitly solving equation (13). More specifically, when $T_{cold} > T_C$ (i.e. the superconductor is in the normal metal regime), the charge current in the forward configuration can be written as:

$$I_N(\Delta V_{th}^{+}, T_N = T_{hot}, T_S = T_{cold}) = \frac{2e}{h}\int_{-\infty}^{\infty} d\epsilon \left[f_N^{+}(\epsilon, \Delta V_{th}^{+}, T_{hot}) - f_S^{+}(\epsilon, 0, T_{cold})\right] T_{AB}(\epsilon), \tag{D.1}$$

where $T_{AB}(\epsilon)$ is the transmission function of the system defined in equation (A.13) of appendix A. Notice that, since the system behaves as an effective N-AB-N device, the current of equation (D.1) takes the standard form for normal metals, which only accounts for the presence of electronic Fermi functions f_N^{+}, f_S^{+} and where the integral goes from $-\infty$ to ∞. Similarly, by inverting the temperatures of the leads, the charge current in the reverse configuration takes the following form:

$$I_N(\Delta V_{th}^{-}, T_N = T_{cold}, T_S = T_{hot}) = \frac{2e}{h}\int_{-\infty}^{\infty} d\epsilon \left[f_N^{+}(\epsilon, \Delta V_{th}^{-}, T_{cold}) - f_S^{+}(\epsilon, 0, T_{hot})\right] T_{AB}(\epsilon). \tag{D.2}$$

It is evident that, due to the non-linearity of the Fermi functions, the value of $|\Delta V_{th}^{+}|$ for which equation (D.1) is equal to zero, is different from $|\Delta V_{th}^{-}|$ obtained setting to zero equation (D.2).

ORCID iDs

Gianmichele Blasi https://orcid.org/0000-0002-4024-788X
Francesco Giazotto https://orcid.org/0000-0002-1571-137X
Géraldine Haack https://orcid.org/0000-0001-7893-0177

References

[1] Fornieri A and Giazotto F 2017 *Nat. Nanotechnol.* **12** 944–52
[2] Pekola J P and Karimi B 2021 *Rev. Mod. Phys.* **93** 041001
[3] Giazotto F, Heikkilä T T, Luukanen A, Savin A M and Pekola J P 2006 *Rev. Mod. Phys.* **78** 217
[4] Yamamoto K and Hatano N 2015 *Phys. Rev.* E **92** 4
[5] Josefsson M, Svilans A, Burke A M, Hoffmann E A, Fahlvik S, Thelander C, Leijnse M and Linke H 2018 *Nat. Nanotechnol.* **13** 920–4
[6] Ono K, Shevchenko S, Mori T, Moriyama S and Nori F 2020 *Phys. Rev. Lett.* **125** 166802
[7] Bernazzani L, Marchegiani G, Giazotto F, Roddaro S and Braggio A 2022 Bipolar thermoelectricity in Bilayer-graphene/superconductor tunnel junctions (arXiv: 2207.08908)
[8] Scharf B, Braggio A, Strambini E, Giazotto F and Hankiewicz E M 2020 *Commun. Phys.* **3** 198
[9] Marchegiani G, Braggio A and Giazotto F 2020 *Phys. Rev.* B **101** 214509
[10] Senior J, Gubaydullin A, Karimi B, Peltonen J T, Ankerhold J and Pekola J P 2020 *Commun. Phys.* **3** 40
[11] Martínez-Pérez M J, Fornieri A and Giazotto F 2015 *Nat. Nanotechnol.* **10** 303–7
[12] Saira O P, Meschke M, Giazotto F, Savin A M, Möttönen M and Pekola J P 2007 *Phys. Rev. Lett.* **99** 027203
[13] Ronzani A, Karimi B, Senior J, Chang Y C, Peltonen J T, Chen C and Pekola J P 2018 *Nat. Phys.* **14** 991–5
[14] Fornieri A, Martínez-Pérez M J and Giazotto F 2014 *App. Phys. Lett.* **104** 183108
[15] Fornieri A, Martínez-Pérez M J and Giazotto F 2015 *AIP Adv.* **5** 053301
[16] Iorio A, Strambini E, Haack G, Campisi M and Giazotto F 2021 *Phys. Rev. Appl.* **15** 054050
[17] Wang H, Hu S, Takahashi K, Zhang X, Takamatsu H and Chen J 2017 *Nat. Commun.* **8** 15843
[18] Roßnagel J, Dawkins S T, Tolazzi K N, Abah O, Lutz E, Schmidt-Kaler F and Singer K 2016 *Science* **352** 325–9
[19] Chand S and Biswas A 2017 *Phys. Rev.* E **95** 032111
[20] Brantut J P, Grenier C, Meineke J, Stadler D, Krinner S, Kollath C, Esslinger T and Georges A 2013 *Science* **342** 713–5
[21] Klatzow J, Becker J N, Ledingham P M, Weinzetl C, Kaczmarek K T, Saunders D J, Nunn J, Walmsley I A, Uzdin R and Poem E 2019 *Phys. Rev. Lett.* **122** 110601
[22] Manzano G, Sánchez R, Silva R, Haack G, Brask J B, Brunner N and Potts P P 2020 *Phys. Rev. Res.* **2** 043302
[23] Ito K and Hayashi M 2018 *Phys. Rev.* E **97** 012129
[24] Yang X, Zheng J and Guo Y 2015 *Physica B: Condens. Matter* **461** 122–8
[25] Sánchez D and López R 2016 *C. R. Physique* **17** 1060–71

[26] Yamamoto K, Entin-Wohlman O, Aharony A and Hatano N 2016 *Phys. Rev.* B **94** 121402
[27] Haack G and Giazotto F 2019 *Phys. Rev.* B **100** 235442
[28] Haack G and Giazotto F 2021 *AVS Quantum Sci.* **3** 046801
[29] Lesovik G B and Sadovskyy I A 2011 *Phys.-Usp.* **54** 1007
[30] Büttiker M, Imry Y and Azbel M Y 1984 *Phys. Rev.* A **30**
[31] Blonder G E, Tinkham M and Klapwijk T M 1982 *Phys. Rev.* B **25** 4515–32
[32] Blasi G, Taddei F, Arrachea L, Carrega M and Braggio A 2021 *Phys. Rev.* B **103** 235434
[33] Lambert C J and Raimondi R 1998 *J. Phys.: Condens. Matter* **10** 901–41
[34] Benenti G, Casati G, Saito K and Whitney R S 2017 *Phys. Rep.* **694** 1–124
[35] Blanter Y M and Büttiker M 2000 *Phys. Rep.* **336** 1–166
[36] Blasi G, Taddei F, Arrachea L, Carrega M and Braggio A 2020 *Phys. Rev. Lett.* **124** 227701
[37] Datta S 1995 *Electronic Transport in Mesoscopic Systems* (Cambridge: Cambridge University Press)
[38] Gresta D, Blasi G, Taddei F, Carrega M, Braggio A and Arrachea L 2021 *Phys. Rev.* B **103** 075439
[39] Andreev A F 1964 *Zh. Eksp. Teor. Fiz.* **46** 1823–8
[40] Pershoguba S S and Glazman L I 2019 *Phys. Rev.* B **99** 134514
[41] Mukhopadhyay A and Das S 2022 Thermal bias induced charge current in a Josephson junction: from ballistic to disordered *Phys. Rev.* B **106** 075421
[42] Hofer P P and Flindt C 2014 *Phys. Rev.* B **90** 235416
[43] Samuelsson P, Kheradsoud S and Sothmann B 2017 *Phys. Rev. Lett.* **118** 256801
[44] Kim T S and Hershfield S 2003 *Phys. Rev.* B **67** 165313
[45] Blasi G, Taddei F, Arrachea L, Carrega M and Braggio A 2020 *Phys. Rev.* B **102** 241302
[46] Büttiker M 1988 *IBM J. Res. Dev.* **32** 63–75
[47] Gefen Y, Imry Y and Azbel M Y 1984 *Phys. Rev. Lett.* **52** 129–32
[48] Tinkham M 1966 *Introduction to Superconductivity* (New York: Mcgraw-Hill)
[49] Kamp M and Sothmann B 2019 *Phys. Rev.* B **99** 045428
[50] Casati G 2007 *Nat. Nanotechnol.* **2** 23–24
[51] Roberts N A and Walker D G 2011 *Int. J. Therm. Sci.* **50** 648–62
[52] Martínez-Pérez M J and Giazotto F 2013 *Appl. Phys. Lett.* **102** 182602
[53] Giazotto F and Bergeret F S 2013 *Appl. Phys. Lett.* **103** 242602
[54] Khandelwal S, Perarnau-Llobet M, Seah S, Brunner N and Haack G 2022 Characterizing the performance of heat rectifiers (arXiv: 2208.10809)
[55] Giazotto F, Grove-Rasmussen K, Fazio R, Beltram F, Linfield E H and Ritchie D A 2004 *J. Supercond.* **17** 317–21
[56] Amado M, Fornieri A, Biasiol G, Sorba L and Giazotto F 2014 *Appl. Phys. Lett.* **104** 242604
[57] Amado M, Fornieri A, Carillo F, Biasiol G, Sorba L, Pellegrini V and Giazotto F 2013 *Phys. Rev.* B **87** 134506
[58] Fornieri A, Amado M, Carillo F, Dolcini F, Biasiol G, Sorba L, Pellegrini V and Giazotto F 2013 *Nanotechnology* **24** 245201
[59] Deon F, Pellegrini V, Giazotto F, Biasiol G, Sorba L and Beltram F 2011 *Phys. Rev.* B **84** 100506
[60] Deon F, Pellegrini V, Giazotto F, Biasiol G, Sorba L and Beltram F 2011 *Appl. Phys. Lett.* **98** 132101
[61] Fornieri A, Martínez-Pérez M J and Giazotto F 2015 *AIP Adv.* **5** 053301